Superior Antibacterial Activity of Fe_3O_4-TiO_2 Nanosheets under Solar Light

Shuanglong Ma, Sihui Zhan,* Yanan Jia, and Qixing Zhou*

Key Laboratory of Pollution Processes and Environmental Criteria (Ministry of Education), College of Environmental Science and Engineering, Nankai University, Tianjin 300071, P. R. China

Ⓢ Supporting Information

ABSTRACT: Fe_3O_4-TiO_2 nanosheets (Fe_3O_4-TNS) were synthesized by means of lamellar reverse micelles and solvothermal method, which were characterized by TEM, XRD, XPS, BET, and magnetic property analysis. It can be found that Fe_3O_4-TNS nanosheets exhibited better photocatalytic antibacterial activity toward Gram-negative *Escherichia coli* and Gram-positive *Staphylococcus aureus* than pure Fe_3O_4 and TNS, and the antibacterial efficiency could reach 87.2% and 93.7% toward *E. coli* and *S. aureus* with 100 μg/mL Fe_3O_4-TNS after 2 h of simulated solar light illumination, respectively. The photocatalytic destruction of bacteria was further confirmed by fluorescent-based cell live/dead test and SEM images. It was uncovered that Fe_3O_4-TNS inactivated G- *E. coli* and G+ *S. aureus* by different mechanisms: the destruction of outer membranes and ruptured cell bodies were responsible for the bactericidal effect against *E. coli*, while the antibacterial effect toward *S. aureus* were due to the fact that the cells were adsorbed in form of clusters by massive Fe_3O_4-TNS, which could restrict their activities and cause malfunction of the selective permeable barriers. Furthermore, the antibacterial mechanism was studied by employing scavengers to understand exact roles of different reactive species, indicating the key roles of h^+ and H_2O_2. The recovery and reusability experiments indicated that Fe_3O_4-TNS still retained more than 90% bacteria removal efficiency even after five cycles. Considering the easy magnetic separation, bulk availability, and high antibacterial activity of Fe_3O_4-TNS, it is a promising candidate for cleaning the microbial contaminated water environment.

KEYWORDS: *photocatalysis, antibacterial, TiO_2 nanosheets, magnetic, E. coli*
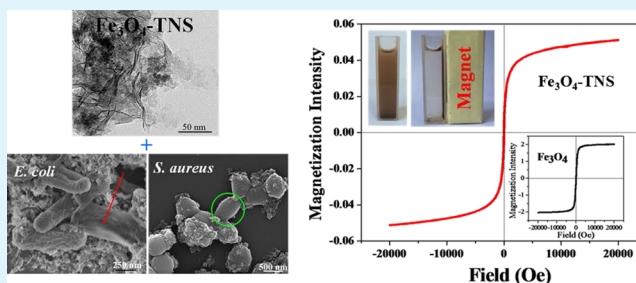
1. INTRODUCTION

Microbial contamination has always been harmful to human health since the existence of human society. Many kinds of bacteria can result in people's serious illness and even death.[1] Therefore, it is significant and necessary to develop effective, low cost, and environmentally benign biocides.[2−4] Since the photon-based disinfection method by platinum-doped TiO_2-mediated photocatalysis was first reported in 1985, photocatalytic disinfection from visible light to ultraviolet light has been extensively investigated.[5,6] Particularly, TiO_2-mediated bacterial inactivation seems to be a preferable technique compared with traditional bacterial inactivation methods such as chlorination and UV methods. Chlorination is not environmentally benign and sustainable because of its carcinogenic disinfection byproducts and the existence of some free chlorine-resistant bacteria such as *Mycobacterium avium*.[7] Additionally, UV light is not effective for some UV-resistant bacteria and the hazards of direct and intensive use of UV radiation restrict its application.[8−10]

As the most popular semiconductor-based photocatalyst, TiO_2 nanomaterials, with different morphology and structure have exhibited great potential applications in the environmental area due to its chemical inertness, lack of toxicity, bulk availability, and strong oxidizing power. However, pure TiO_2 nanoparticles have their inherent disadvantages such as large band gap, easy recombination of charge carriers, hard to be separated, and constant aggregation in solution. Since a series of excellent properties of graphene have been demonstrated, enormous efforts have been made to study other inorganic ultrathin nanosheets with mono- and multiatomic layers such as MoS_2, TiS_2, TiO_2, and so on.[11] Recently, two-dimensional transition metal oxides exhibit promising applications in electrocatalysis, electronic devices, and energy storage for the characteristics of intrinsic quantum confined electrons.[12] The TiO_2 nanosheets (TNS) features with confined thickness and dramatically increased surface area provide a great opportunity for developing novel photocatalysts[13,14] and lithium-ion batteries.[15−17] It has been demonstrated that TiO_2 nanosheets have higher specific surface area and faster interfacial electron transfer rates than P25.[18,19] These ultrathin 2D TiO_2 nanosheets exhibited unusual exposed facets, high-energy {010} facets, which were demonstrated to be vital for

enhancing their chemical activity.[12] Two-dimensional TiO_2 nanosheets with high surface area and numerous surface hydroxyl groups were expected to be ideal materials for environmental remediation.[18,20]

On the other hand, it is necessary and difficult to separate effectively used nanomaterials from the heterogeneous system to avoid secondary pollution and recycled nanomaterials.[21−23] Although traditional separation strategies such as centrifugation, free settling, and filtration have been widely adopted, they suffer from loss of catalysts, complicated operating equipment, and high operational costs.[24] Therefore, a benign, effective, and inexpensive separation method is extremely desirable. Compared with the above separation methods, magnetic separation shows superior separation effect because of its low cost and easy operation. Many magnetic nanoparticles, functionalized with bioprotein,[25] amino acid,[26] antibody,[27] and carbohydrates[28] were applied to target bacteria capture and detection. Therefore, a promising solution for separating TiO_2 after environmental application is to synthesize the TiO_2/Fe_3O_4 nanocomposite. Some similar strategies including Au-decorated $Fe_3O_4@mTiO_2$ core−shell microspheres,[29] $Ag_3PO_4/TiO_2/Fe_3O_4$ heterostructure,[30] and Fe_3O_4/TiO_2 core/shell magnetic nanoparticles[31] have been reported for photocatalytically inactivate pathogenic bacteria.

In this work, for achieving better disinfection effect, untrathin Fe_3O_4-TiO_2 nanosheets (Fe_3O_4-TNS) composite, which combined the photocatalytic disinfection activity of TNS and magnetic separation property of Fe_3O_4, were successfully synthesized by the solvothermal method.[12,32] The Fe_3O_4-TNS nanosheets were then characterized by TEM, SEM, XRD, FTIR, XPS, BET, and magnetic property analysis. The antibacterial effects of Fe_3O_4-TNS in the presence/absence of simulated solar irradiation and with/without magnetic separation were systematically investigated. Fe_3O_4-TNS nanosheets exhibited higher photocatalytic sterilization and bacteria removal efficiency than TNS and Fe_3O_4, which is due to their large surface area, higher absorption in the visible light region, and lower recombination ratio of photogenerated electron−hole pairs.

2. EXPERIMENTAL SECTION

2.1. Materials. All chemicals used in this work are analytical grade. All chemicals were used without any further purification. Titanium isopropoxide (TTIP) was purchased from Aladdin Corperation (Shanghai, China). Poly(ethylene glycol)$_{20}$-*block*-poly(propylene glycol)$_{70}$-*block*-poly(ethylene glycol)$_{20}$ (Pluronic P123) was purchased from Sigma-Aldrich (St. Louis, Missouri). Anhydrous ethanol (C_2H_5OH), ethylene glycol (EG), ferric chloride hexahydrate ($FeCl_3·6H_2O$), and sodium acetate anhydrate (NaAc) were purchased from Jiangtian Chemical Technology Co. Ltd. (Tianjin, China).

2.2. Synthesis and Characterization of Fe_3O_4-TNS. 4.2 g of TTIP was added into 2.96 g of concentrated HCl solution under vigorous stirring, and 0.8 g of Pluronic P123 was dissolved with 12.0 g ethanol by a magnetic stirrer for 30 min. Then the above solution was added into TTIP solution. After 45 min agitation, 10 mL of the above mixture solution was added into 80 mL of EG and then transferred to a Teflon-lined autoclave. The autoclave was heated in an oven at 150 °C for 20 h and then cooled down to room temperature. The obtained white samples were washed several times using distilled water and ethanol and dried at 80 °C for 24 h.

Then, 1.0 g of TNS was dispersed under ultrasonication in 160 mL of EG for 30 min. 3.2 g $FeCl_3·6H_2O$ and 6.4 g NaAc were added in the above TNS solution with agitation for 30 min. Then the solution was transferred into a Teflon-lined autoclave and heated in an oven at 200 °C for 6 h. After cooling down to room temperature, the obtained

black composite was washed several times with ethanol. Finally, the product was dried in an oven at 60 °C for 24 h. As a comparison, the Fe_3O_4 was synthesized the same way as the above method apart from the addition of TNS.

The X-ray diffraction (XRD) patterns were recorded via an X-ray diffractometer (Rigaku D/Max 2500PC) with a Cu Kα radiation. The morphology and elemental analysis were observed through transmission electron microscopy (TEM, JEOL Model JEM-1200EX). The morphology of bacteria was imaged by scanning electron microscopy (Hitachi S-4800, Japan). X-ray photoelectron spectroscopy (XPS) spectra were collected on an ESCALAB250 multitechnique X-ray photoelectron spectrometer using a monochromatic Al Kα X-ray source. Light absorption (reflectance) spectra were recorded by UV−vis−NIR diffuse reflectance spectrum (Shimadzu Corporation, UV-3600, Japan). N_2 adsorption−desorption data were obtained using a Quantachrom SI Micromeritics apparatus, and the isotherms were evaluated with the Barrett−Joyner−Halenda (BJH) theory. The magnetic properties of the nanoparticles were investigated using a vibrating sample magnetometer (LDJ 9600-1, USA) at room temperature by cycling the field from −2 to 2 kOe.

2.3. Antibacterial Activity. Gram-negative *E. coli* and Gram-positive *S. aureus* were used as model bacteria. The bacteria were grown in nutrient broth at 37 °C for 15 h to yield a cell count of approximately 10^9 colony forming units (CFU)/mL. Then bacterial cells were collected by centrifugation (5000 × g for 10 min) and resuspended in sterile 0.85% (wt/vol) saline solution. The bacteria level for bactericidal study was 10^7 CFU/mL, which was adjusted by gradient dilution using a 0.85% (wt/vol) saline solution.

Typically, 75 μL of samples suspended in saline solution were added to 3 mL of bacteria solution, leading to different ultimate concentrations of materials including 12.5, 25, 50, and 100 μg/mL. The bacteria and materials were mixed at 180 rpm in a rotary shaker at room temperature and simultaneously irradiated by a 300 W xenon arc lamp (CEL-HXF300, Ceaulight, Beijing) for 2 h. Then the nanomaterials were magnetically separated for 10 min with an external magnet. The supernatant was carefully pipetted out, and bacteria concentrations were determined by the standard plate count method. The plates were incubated at 37 °C for 24 h. The number of colonies was enumerated through visual inspection. There were a series of experiments conducted without irradiation at the same situations as the dark control. To investigate the magnetic separation effect and the adsorption capacity of these photocatalysts, a group of experiments were conducted in the same situation except that the number of bacteria was counted without separating the materials. The light control group was carried out in the absence of a photocatalyst.

2.4. Fluorescent-Based Cell Live/Dead Test. The bacteria death analysis was also ascertained by fluorescent-based cell live/dead test. The mixture of log phase cells (10^7 CFU/mL) and nanosheets (100 μg/mL) were incubated in a rotary shaker at 180 rpm for 2 h under irradiation. Then the mixture were stained with PI (propidium iodide) and SYTO9 (LIVE/DEAD Baclight Bacterial Viability kit) according to the instruction of the kit and imaged using a laser scanning fluorescence microscopy (Olympus, FV1000). The cell suspension irradiated under light without photocatalyst was taken as the control.

2.5. SEM Observation of Bacteria. SEM was used to visualize the interaction between Fe_3O_4-TNS and bacteria. The bacteria treated with Fe_3O_4-TNS were fixed on a silicon pellet with 2.5% glutaraldehyde solution in 4 °C overnight. Then the samples were sequentially dehydrated with 30, 50, 70, 90, and 100% ethanol for 20 min, respectively. Then, the samples were lyophilized, gold sputter-coated, and observed.

3. RESULTS AND DISCUSSION

3.1. Characterizations of Photocatalysts. The typical TEM and SEM images of TNS and Fe_3O_4-TNS were shown in Figure 1. The ultrathin TNS existed in the form of groups of nanosheets, and there were curls in the edges of TNS because of surface tension which was similar to the property of graphene (Figure 1a,d).[12] From the SEM images, Fe_3O_4-TNS
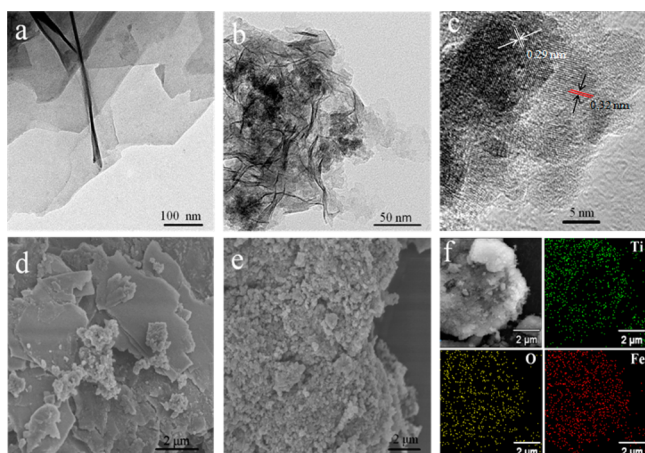
Figure 1. TEM images of (a) TNS, (b) Fe$_3$O$_4$-TNS, (c) HRTEM of Fe$_3$O$_4$-TNS, (d) SEM images of TNS, (e) Fe$_3$O$_4$-TNS, and (f) elemental map of Fe$_3$O$_4$-TNS obtained by EDS.

was not so smooth as TNS due to the deposition of Fe$_3$O$_4$ nanoparticles (Figure 1, panels b and e). The HRTEM of Fe$_3$O$_4$-TNS shown in Figure 1c revealed the lattice fringes of TiO$_2$ (d = 0.32 nm) and Fe$_3$O$_4$ (d = 0.29 nm), indicating that TiO$_2$ and Fe$_3$O$_4$ samples were highly crystalline. Energy dispersive spectroscopy (EDS) of Fe$_3$O$_4$-TNS was conducted to provide a two-dimensional elemental distribution (Figure 1f). A brighter area in the elemental map indicated a higher concentration of the corresponding element in that area.[33] Different elements were displayed in different colors in order to identify their positions within the nanomaterials. It was obvious that different elements including O, Ti, and Fe were distributed uniformly within the nanocomposite.

In the XRD patterns (Figure S1), the pentagram represented characteristic peaks of crystal Fe$_3$O$_4$. It was obvious that the diffraction peaks appearing at 2θ = 18.2°, 30.0°, 35.3°, 42.9°,

53.4°, and 56.9° could be indexed to (111), (220), (311), (422), (511), and (440) planes of the cubic phase Fe$_3$O$_4$ (JCPDS no. 89-4319), respectively.[32] As shown in Figure S1, the circle represented characteristic peaks of crystal TiO$_2$. The peaks appearing at 25.4° (101), 37.9° (004), and 48.0° (200) could be attributed to anatase phase of TiO$_2$. However, these peaks appearing at 27.5° (110), 44.0° (210), 56.7° (220), and 62.8° (002) were ascribed to the rutile phase of TiO$_2$. Therefore, TNS exhibited a mischcrystal of anatase and rutile.[12]

To further study the micro component of Fe$_3$O$_4$-TNS and observe the valence of different elements, the XPS spectra of Fe$_3$O$_4$-TNS were shown in Figure 2a and Figure S2. In Figure 2a, the three different major peaks were assigned to Fe 2p, O 1s, and Ti 2p. In Fe 2p spectrum (Figure S2a), the binding energies of 725.1 and 710.9 eV were indexed to Fe 2p$_{1/2}$ and Fe 2p$_{3/2}$, respectively, indicating the formation of the Fe$_3$O$_4$ phase in the composite.[29] As shown in Figure S2b, the O 1s XPS spectrum of Fe$_3$O$_4$-TNS could be separated into three spectral components, including C=O (531.3 eV), Fe–O (530.1 eV), and Ti–O (529.6 eV). From Figure S2c, the two peaks at 464.3 and 458.5 eV corresponded to Ti 2p$_{1/2}$ and Ti 2p$_{3/2}$, respectively.[19] All the above analyses further verified the combination of Fe$_3$O$_4$ nanoparticles with TNS.

The N$_2$ adsorption−desorption isotherms and the pore diameter distribution of Fe$_3$O$_4$, TNS, and Fe$_3$O$_4$-TNS were exhibited in Figure 2 (panels b and c), and the data of the surface area, pore size distribution, and pore volume were listed in Table S1. From Figure 2b, Fe$_3$O$_4$ showed typical type II curve without the hysteresis loop, suggesting its nonporous microstructure. However, TNS and Fe$_3$O$_4$-TNS exhibited the typical IV type isotherms with the hysteresis loop in 0.4−1.0 and 0.4−0.9 range of relative pressure, respectively, suggesting that well porous structures were formed in TNS and Fe$_3$O$_4$-TNS. The BJH pore size distributions of TNS and Fe$_3$O$_4$-TNS had the porous diameters of maximum distribution, 37.3 and 75.0 nm, respectively, indicating the bigger pore diameter of
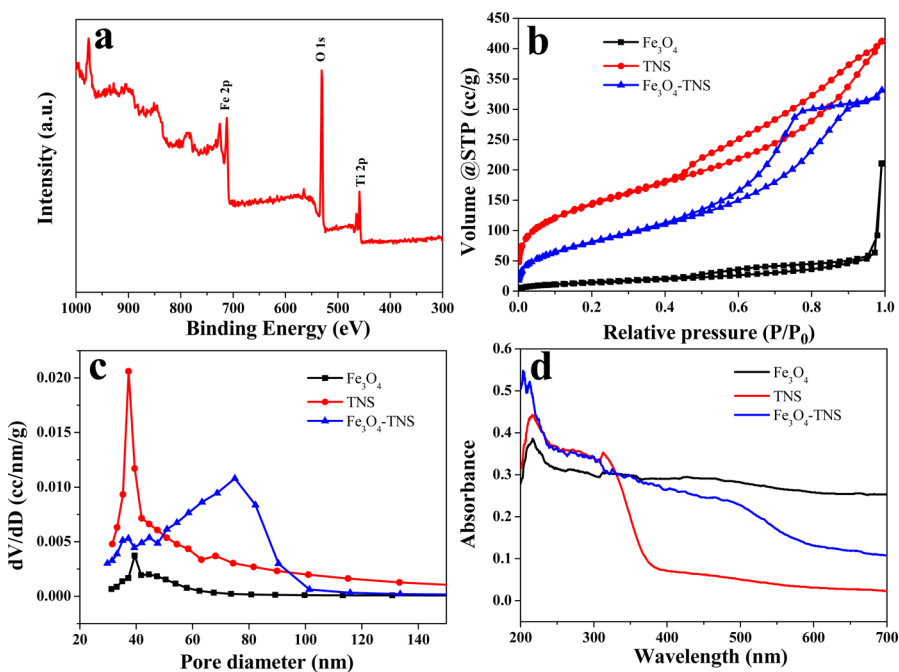

Figure 2. XPS spectrum of (a) Fe$_3$O$_4$-TNS, (b) N$_2$ adsorption−desorption isotherms, (c) pore size distributions, and (d) UV−vis spectra of Fe$_3$O$_4$, TNS, and Fe$_3$O$_4$-TNS.
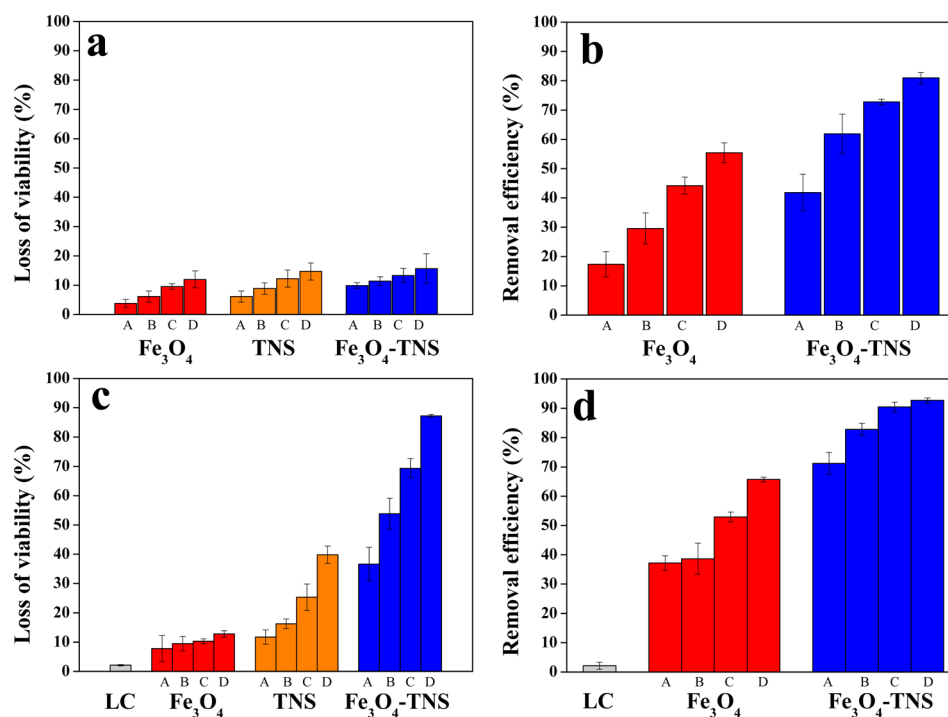
Figure 3. Loss of viability of *E. coli* (10^7 CFU/mL) under (a and b) dark and (c and d) simulated solar irradiation (a and c) without and (b and d) with magnetic separation after treating with Fe_3O_4, TNS, and Fe_3O_4-TNS at different concentrations. A, B, C, and D represent the final concentrations of different materials at 12.5, 25, 50, and 100 μg/mL, respectively.

Fe_3O_4-TNS. The surface areas of Fe_3O_4, TNS, and Fe_3O_4-TNS were 56.5, 513.2, and 295.8 m^2/g, respectively. The surface area of TNS was decreased after Fe_3O_4 modification. It was possibly attributed to the fact that the TiO_2 nanosheets curled and stacked together during the solvothermal synthesis process of Fe_3O_4-TNS, which could also be demonstrated by the TEM images of TNS and Fe_3O_4-TNS (Figure 1, panels a and b). In addition, part of adsorption sites on the surface of TNS may be taken up by formed Fe_3O_4 nanoparticles. Although TNS had a higher surface area than Fe_3O_4-TNS, the surface area was not the only factor that affected the photocatalytic activity. In accordance with the superior antibacterial effect of Fe_3O_4-TNS compared with TNS, the Fe_3O_4 nanoparticles on the surface of TNS, which could trap the electron and promote the separation of electron−hole pairs, were considered the significant factor affecting the photocatalytic activity. The surface area of Fe_3O_4-TNS was higher than the reported value of Fe_3O_4−TiO_2 with a core−shell structure of about 139.8 m^2/g.[33] It was well-accepted that the specific surface area of the photocatalyst had obviously positive correlation with the quantity of active reaction sites on its surface.[34,35] Compared with the core−shell structure, the high specific surface area of the Fe_3O_4-TNS nanocomposites would guarantee their extremely high adsorption and photocatalytic capacity.

To understand the optical properties of as-prepared samples, the UV−visible diffuse reflectance spectra (UV−vis DRS) were conducted (Figure 2d). It was obvious that the TNS absorbed light with wavelengths mainly below 400 nm. In contrast to TNS, the absorption edge of Fe_3O_4-TNS shifted toward longer wavelength, which was attributed to the deposition of Fe_3O_4 nanoparticles on the TNS plane. Fe_3O_4-TNS had absorption in the visible region, ranging from 400 to 700 nm, suggesting that Fe_3O_4-TNS had a higher photocatalytic antibacterial effect under solar light irradiation.

As shown in Figure S3, the hysteresis loop indicated that the magnetic saturation (Ms) value of the Fe_3O_4-TNS nanocomposite was 0.05 emu/g, which was lower than that of Fe_3O_4 nanoparticles (2.02 emu/g) exhibited in the bottom right inset of Figure S3, which was possibly attributed to reduced relative content of Fe_3O_4 in Fe_3O_4-TNS nanocomposites.[36] Although the magnetic saturation value of the Fe_3O_4-TNS was lower than that of pure Fe_3O_4, the top left inset of Figure S3 suggested that Fe_3O_4-TNS nanocomposites could still be easily separated from solution with an external magnet. The rapid and simple separation of Fe_3O_4-TNS from water after application was significant not only for reusing the photocatalyst but also for avoiding second environmental pollution.

3.2. High Antibacterial Performance of Fe_3O_4-TNS. As shown in Figure 3, Fe_3O_4, TNS, and Fe_3O_4-TNS showed antibacterial effect toward *E. coli* in a dose-dependent manner. In the dark, the antibacterial percentage was less than 10%, indicating that Fe_3O_4, TNS, and Fe_3O_4-TNS showed negligible cytotoxicity toward *E. coli*, which was in accordance with these results in the earlier reports.[37,38] After magnetic separation, the bacterial removal efficiency of Fe_3O_4 and Fe_3O_4-TNS was 55.4% and 80.9% at a material concentration of 100 μg/mL in the dark, respectively (Figure 3b). In the dark, the removed bacteria could be divided into two parts: the dead bacteria due to the very low cytotoxicity of Fe_3O_4 and Fe_3O_4-TNS to *E. coli* (below 10%) and the live bacteria adsorbed by them. Obviously, the adsorption activity contributed to the most proportion of the removal percentage. In addition, the Fe_3O_4-TNS showed about 25% of higher adsorption efficiency than Fe_3O_4. It was the higher specific surface area of Fe_3O_4-TNS that should be responsible for its better adsorption efficiency. As shown in Figure 3c, without magnetic separation, the antibacterial percentage of Fe_3O_4, TNS, and Fe_3O_4-TNS was 12.8%, 39.8%, and 87.2% at a material concentration of 100 μg/
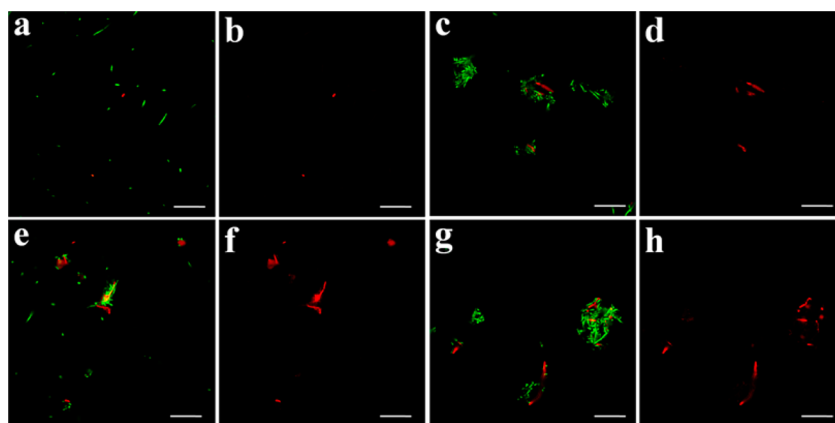
Figure 4. Confocal fluorescent images of live and dead *E. coli* (10^7 CFU/mL) of (a and b) light control, (c and d) treatments added with 100 μg/mL of Fe_3O_4, (e and f) TNS and (g and h) Fe_3O_4-TNS stained with SYTO9 (green) and PI (red). (a, c, e, and g) overlying images of *E. coli* stained with SYTO9 (live and dead) and PI (dead). (b, d, f, h) images of *E. coli* stained with PI. The scale bar is 20 μm.

mL after 2 h of simulated solar light illumination, respectively. With magnetic separation, Fe_3O_4 and Fe_3O_4-TNS exhibited 65.7% and 92.7% of bacterial removal percentage (Figure 2d). Moreover, these removed bacteria included two kinds of conditions: the dead bacteria which were photocatalytic disinfected and the live bacteria which were just adsorbed. It was obvious that most of the bacteria were photokilled by Fe_3O_4-TNS, and only about 5% of bacteria were just adsorbed. Noticeably, Fe_3O_4-TNS in different levels always possessed the best bacterial removal efficiency compared with pure Fe_3O_4 and TNS.

As is well-known, there are many different kinds of pathogenic bacteria in wastewater. To assess the antibacterial effect of Fe_3O_4-TNS to different kinds of bacteria, G- *E. coli* and G+ *S. aureus* were taken as model organisms. As shown in Figure S4 (panels a and b), for Fe_3O_4-TNS, the antibacterial efficiency increased rapidly with the extension of irradiation time in the first 30 min and reached 58.2% and 60.5% against *E. coli* and *S. aureus* after 30 min, respectively. Within 60 min, 72.3% of *E. coli* and 75.8% of *S. aureus* had been inactivated, suggesting that Fe_3O_4-TNS exhibited efficient antibacterial activity, which was significant for the microbial pollution emergency. At the end of the photocatalytic disinfection, the antibacterial efficiency reached 87.2% and 93.7% toward *E. coli* and *S. aureus*, respectively. The pH influence was evaluated because the solution pH was a vital factor affecting the absorption and photocatalytic process.[39] As shown in Figure S4c, the pH value played an important role toward *E. coli* removal. After 2 h of exposure, for Fe_3O_4-TNS (100 μg/mL), the removal percentage of *E. coli* decreased with the increase of the pH value, and the removal percentage was 97.6%, 92.7%, and 46.0% at pH value of 5, 7, and 9, respectively, indicating that *E. coli* could easily be adsorbed at low pH value. It was the negative charged bacterial membrane that should be responsible for this difference.[40]

3.3. Fluorescent-Based Cell Live/Dead Test. In addition to the standard CFU counting method, fluorescent-based cell live/dead test was conducted by a laser scanning fluorescence microscopy to verify the antibacterial effect. SYTO9 and PI, two fluorescent nucleic acid dyes, were employed to stain the DNA of *E. coli*. SYTO9 was a cell-permeable green-fluorescent stain labeled both live and dead bacteria, whereas PI was a cell-impermeable red-fluorescent stain that only labeled cells with compromised cellular membranes. As shown in Figure 4

(panels a and b), there were few dead cells and the cells exhibited uniform dispersity in the light control. For the Fe_3O_4 treatment (Figure 4, panels c and d), the bacteria aggregated together and only a small number of cells were dead. However, for TNS, the cells which were adsorbed on the materials exhibited red fluorescence after PI staining, and the cells without agglomerated together were still live. For Fe_3O_4-TNS treatment, there were a large proportion of bacteria which were photokilled by the Fe_3O_4-TNS, and most of the bacteria exhibited agglomerate state. It was the better adsorption and antibacterial capacity of Fe_3O_4-TNS that should be responsible for this phenomenon.

3.4. Cell Integrity Destruction Induced by Fe_3O_4-TNS. From Figure S4, it was found that Fe_3O_4-TNS presented different antibacterial effects against *E. coli* and *S. aureus*. It is generally accepted that destruction of the outer wall and membrane of bacteria is a crucial process for disinfection. However, the Gram negative *E. coli* and positive *S. aureus* have a different cell wall and membrane structure including the outermost lipopolysaccharide layer found only in *E. coli*, the peptidoglycan multilayer layer presented in both *E. coli* (15–20 nm) and *S. aureus* (20–80 nm), and the phospholipid layer in *E. coli* (bilayer) and *S. aureus* (monolayer).[41]

In order to investigate the respective antibacterial mechanism and bacterial morphological change, both bacterial cells were visualized using SEM technology. Before irradiation, *E. coli* exhibited intact and smooth membranes as well as normal rhabdoid morphology (Figure 5a). After only a 15 min-exposure, the adsorbed *E. coli* had become deformed (Figure 5b), which indicated that the active species including h^+, H_2O_2, and $\bullet O_2^-$ had been rapidly produced, contacted with the out membrane of the cell. As shown in Figure 5c, it was obvious that *E. coli* cells were fixed on the TiO_2 plane and fused into the material after 30 min irradiation. Remarkably, the cells became longer and some of them were even drilled, forming big cavities on surfaces, which possibly attributed to the attacks of different reactive species. As the illumination extended to 60 min (Figure 5d), the *E. coli* cells further became longer and extremely deformed. Cell elongation was a typical SOS response of cell under detrimental situations such as exposure to biocides and UV irradiation.[42–44] As shown in Figure 5e, after 2 h of irradiation, the cell shape was seriously distorted and the cell membrane was greatly ruptured, which promoted the entrance of reactive species and further degraded the left intracellular
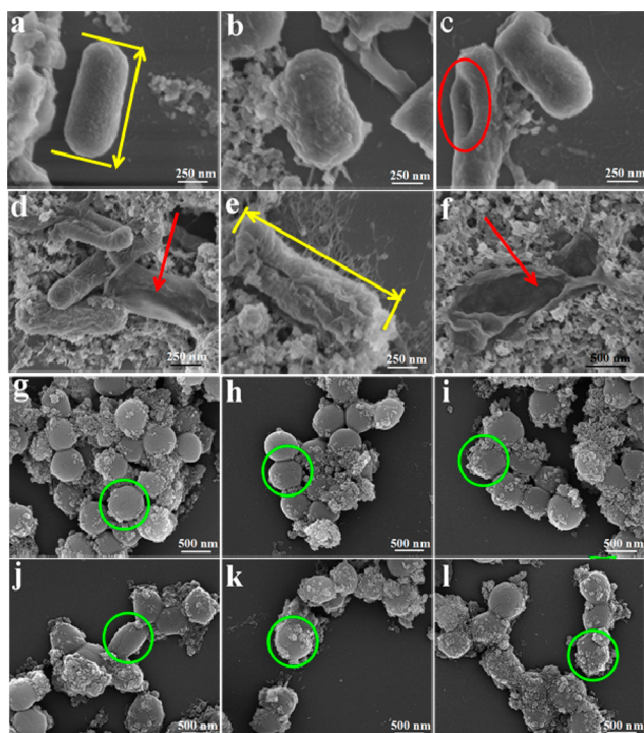
Figure 5. SEM images of (a−f) *E. coli* and (g−l) *S. aureus* treated with Fe$_3$O$_4$-TNS (100 μg/mL) under solar light. (a and g) 0 min, (b and h) 15 min, (c and i) 30 min, (d and j) 60 min, (e and k) 120 min, and (f and l) 240 min. The yellow double arrows and lines are intended to measure the length of *E. coli*. The ellipse and red arrows indicate the deformation, pore-forming, and fracture of *E. coli*. The green circles indicate the shape variation of *S. aureus* during the antibacterial process.

Figure 6. (a) Photoluminescence (PL) spectra and (b) transient photocurrent of TNS and Fe$_3$O$_4$-TNS.

components. The *E. coli* cells were totally distorted after 4 h of irradiation as exhibited in Figure 5f.

However, for *S. aureus*, there was no obvious cell wall and membrane destruction during the whole disinfection process (Figure 5, panels g−l). It could be observed that morphology of *S. aureus* cells changed from regular sphere to irregular shape over the illumination time. In addition, the *S. aureus* had a smaller diameter compared with *E. coli*, and they were inclined to gather with each other. Obviously, they were adsorbed by Fe$_3$O$_4$-TNS in the form of a cluster compared with *E. coli*. Although the membranes of *S. aureus* cells were difficult to be ruptured by reactive species for their rigid membrane structure, their surfaces were covered by massive Fe$_3$O$_4$-TNS which could restrict their activities and cause malfunction of the selective permeable barriers and further the death of cells.

3.5. Mechanism of Enhanced Photocatalytic Antibacterial Effect of Fe$_3$O$_4$-TNS. Generally, Fe$_3$O$_4$ was considered as an excellent conductor for its high conductivity (1.9 × 10^6 S m^{-1}), which could trap the photoinduced electrons and further enhance the separation and transportation of electron−hole pairs. Photoluminescence spectra (PL spectra) were conducted to investigate the migration, transfer, and recombination processes of photogenerated electron−hole pairs. The PL spectra of TiO$_2$ nanosheets (TNS) and Fe$_3$O$_4$-TNS composite at the excitation wavelength of 320 nm were exhibited in Figure 6a. Their emission bands positioned at 470−500 nm. The emission intensity of the Fe$_3$O$_4$-TNS could almost be ignored compared with that of TNS, indicating that incorporation of Fe$_3$O$_4$ reduced the charge recombination rate
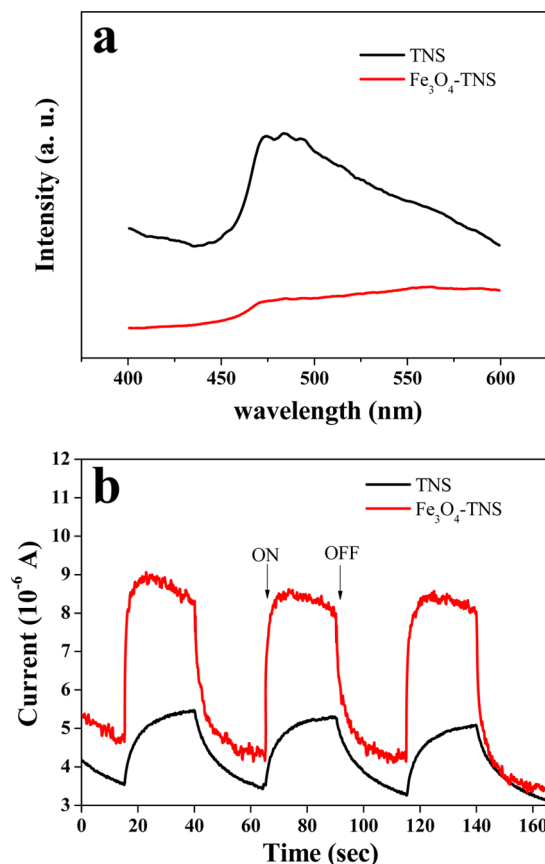
due to efficient transfer of photoexcited electrons from the conduct band of TNS to Fe$_3$O$_4$.[45] The photocurrent was formed mainly by separation and diffusion of photogenerated electrons and holes from the inner structure of photocatalyst to the free charge acceptors on its surface and in the electrolyte. As shown in Figure 6b, the photocurrent response of the Fe$_3$O$_4$-TNS was much higher than TNS under simulated solar light irradiation, indicating that there were less recombination and more efficient separation of photoinduced electron−hole pairs in the Fe$_3$O$_4$-TNS composite. Obviously, the photocurrent curve of Fe$_3$O$_4$-TNS was different from TNS. Compared with TNS, the photocurrent of Fe$_3$O$_4$-TNS quickly reached the peak value when the light was turned on. Then the photocurrent maintained steady during the illumination. However, that of TNS increased slowly to the peak value indicating that the separation rate of photoinduced electron−hole pairs of Fe$_3$O$_4$-TNS was faster than TNS. All of these suggested that Fe$_3$O$_4$ could effectively trap photoinduced electron and facilitate the separation of electron−hole pairs, which could account for the better antibacterial effect of Fe$_3$O$_4$-TNS.

3.6. Photocatalytic Disinfection Mechanism. During photocatalytic disinfection process, the h$^+$, ·OH, H$_2$O$_2$, and ·O$_2^-$ were usually considered to be the reactive oxidative species responsible for the bactericidal activity.[6] Understanding which species played the most prominent role was significant for improving the antibacterial effect. However, for different photocatalytic systems, the determining species may be different. The scavengers, including Cr(VI) for electron,[46] isopropanol for ·OH,[47] sodium oxalate for hole,[48] and Fe(II)

for H_2O_2,[49] were used to investigate the exact roles of these reactive species. Before conducting scavenger experiments, the applied concentration of different scavengers were determined to eliminate their influence on *E. coli*. The pH value of the mixture without scavengers was about 7.02 and changed from 6.71 to 7.23 after the addition of scavengers. According to the early report, this change had no obvious influences on the photocatalytic disinfection.[50] As shown in Figure 7a, compared
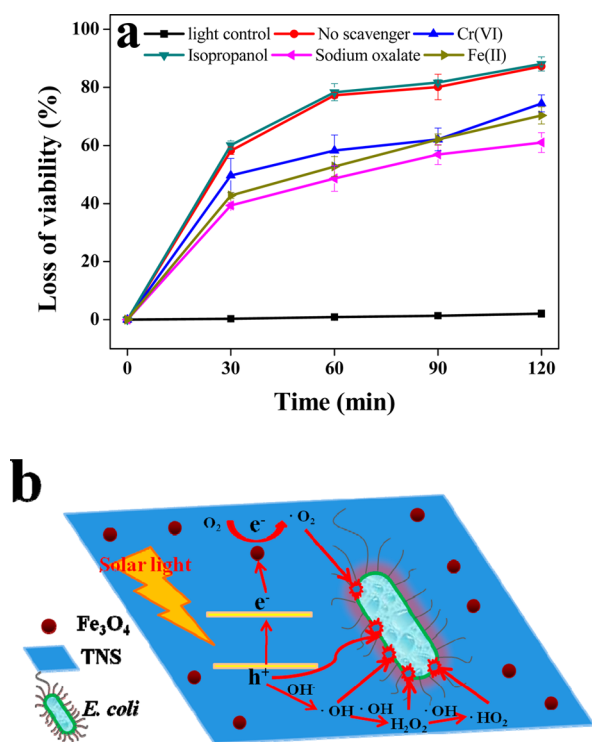

Figure 7. (a) Photocatalytic antibacterial efficiency against *E. coli* (10^7 CFU/mL) in the presence of Fe_3O_4-TNS (100 μg/mL) with different scavengers [0.05 mmol/L Cr(VI), 0.5 mmol/L isopropanol, 0.5 mmol/L sodium oxalate, and 0.1 mmol/L Fe(II)-EDTA] under simulated solar light and (b) mechanism of the photocatalytic disinfection of *E. coli* by Fe_3O_4-TNS under solar light.

with that of no scavenger, the disinfection efficiency had changed little after the addition of isopropanol to remove •OH, indicating that •OH was not a crucial reactive species in this photocatalytic process. With the addition of Cr(VI) to combine e^-, the antibacterial percentage decreased to 74.5%, suggesting the important role of e^- because they possibly transformed into other reactive species such as •O_2^- and H_2O_2, which could oxidize the out membrane of bacteria. The inhibition of photocatalytic antibacterial activity occurred in the presence of Fe(II), which removed H_2O_2. The antibacterial percentage declined to 70.3% after 2 h of irradiation, further indicating that H_2O_2 had an important impact on the antibacterial process. Noticeably, in the presence of sodium oxalate, the antibacterial efficiency of Fe_3O_4-TNS fell to 61.0% after 2 h irradiation, suggesting that the h^+ generated at the oxidation site of Fe_3O_4-TNS was the most important reactive species during the photocatalytic antibacterial process. As shown in Figure 7b, h^+ could react with surface adsorbed hydroxyl groups (OH^-) or water to produce a surface adsorbed hydroxyl radical.[39] Therefore, the major reactive species for the simulated solar

photocatalytic inactivation by Fe_3O_4-TNS could be h^+ and H_2O_2.

3.7. Reusability of Fe_3O_4-TNS. The recovery and reusability were considerable for the application of the nanostructured photocatalysts in water remediation. The rapid and convenient separation of Fe_3O_4-TNS from water after application was significant not only for reusing but also for avoiding second pollution. To investigate the reusability of Fe_3O_4-TNS, the materials were collected by a magnet after photocatalytic disinfection. The recovery materials were dispersed by ultrasonication in 75% of ethanol aqueous solution for 30 min to decompose the captured bacteria and then rested in room temperature overnight. After magnetic separation, the materials were washed thoroughly with sterile 0.85% (wt/vol) saline solution prior to the next cycle (Figure S5 and Figure S6). As shown in Figure 8, the bacteria removal
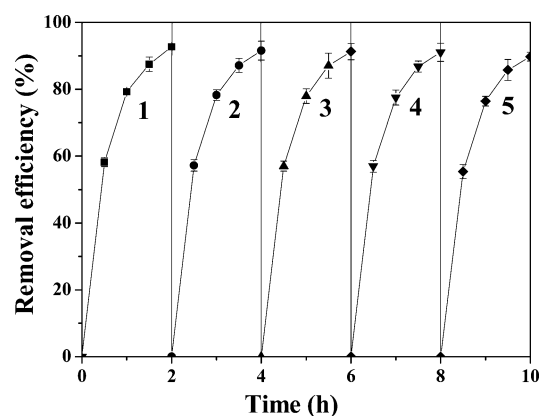

Figure 8. Removal efficiencies against *E. coli* (10^7 CFU/mL) in the presence of Fe_3O_4-TNS (100 μg/mL) in five cycles under simulated solar light.

efficiency decreased with the increase of recycling times, possibly due to the loss of photocatalyst during separation and purification, and the contamination of photocatalyst surface by bacteria residues. Although the bacteria removal efficiency exhibited a slight decrease with the increasing cycles, more than 90% of *E. coli* strains could be removed by Fe_3O_4-TNS, even in the fifth cycle.

4. CONCLUSIONS

In this paper, Fe_3O_4-TiO_2 nanosheets (Fe_3O_4-TNS) composites were synthesized by lamellar reverse micelles and a solvothermal method for efficient antibacterial application, which were characterized by TEM, XRD, XPS, BET, and magnetic property tests. It could be found that Fe_3O_4-TNS exhibited the superior antibacterial efficiency compared with Fe_3O_4 and TNS nanomaterials, which was due to the unique heterojunction in Fe_3O_4-TNS. The SEM images revealed the possibly different antibacterial mechanism of *E. coli* and *S. aureus*. For *E. coli*, the cell bodies were easily distorted and ruptured by reactive species. However, for *S. aureus*, there were no obvious membrane destruction, and the cell surfaces were covered by massive Fe_3O_4-TNS, which could restrict their activities and cause malfunction of the selective permeable barriers and further the death of cells. The electrochemical methods including PL spectra and photocurrent were employed to explain the mechanism of enhanced antibacterial efficiency after Fe_3O_4 modification, suggesting that Fe_3O_4 could

effectively trap the photoinduced electron and facilitate the separation of electron−hole pairs. The results of scavengers experiment indicated that the major reactive species for disinfection by Fe_3O_4-TNS could be h^+ and H_2O_2. The Fe_3O_4-TNS exhibited more than 90% of removal efficiency toward *E. coli* even after five recycles. Therefore, taking into account its easy magnetic separation, bulk availability, and high antibacterial activity, Fe_3O_4-TNS is an ideal photocatalyst for advanced pathogenic bacteria wastewater treatment.

■ ASSOCIATED CONTENT

Ⓢ Supporting Information

The Supporting Information is available free of charge on the ACS Publications website at DOI: 10.1021/acsami.5b06264.

> XRD, XPS spectrum; room temperature magnetization curves; the influences of time and pH on the antibacterial percentage; specific area, pore volume, and pore diameter distribution; the morphology change of Fe_3O_4-TNS after antibacterial application (PDF)

■ AUTHOR INFORMATION

Corresponding Authors

*E-mail: sihuizhan@nankai.edu.cn. Tel: +86-022-23507800. Fax: +86-022-66229562.
*E-mail: zhouqx@nankai.edu.cn.

Notes

The authors declare no competing financial interest.

■ ACKNOWLEDGMENTS

■ REFERENCES

(1) Philip, S. S.; Costerton, J. W.; Greenberg, E. P. Bacterial Biofilms: A Common Cause of Persistent Infections. *Science* **1999**, *284*, 1318−1322.

(2) Ma, S. L.; Zhan, S. H.; Jia, Y. N.; Zhou, Q. X. Highly Efficient Antibacterial and Pb(II) Removal Effects of Ag-CoFe₂O₄-GO Nanocomposite. *ACS Appl. Mater. Interfaces* **2015**, *7*, 10576−10586.

(3) Podporska-Carroll, J.; Panaitescu, E.; Quilty, B.; Wang, L. L.; Menon, L.; Pillai, S. C. Antimicrobial Properties of Highly Efficient Photocatalytic TiO₂ Nanotubes. *Appl. Catal., B* **2015**, *176-177*, 70−75.

(4) Romero-Maraccini, O. C.; Sadik, N. J.; Rosado-Lausell, S. L.; Pugh, C. R.; Niu, X. Z.; Croue, J. P.; Nguyen, T. H. Sunlight-Induced Inactivation of Human wa and Porcine OSU Rotaviruses in the Presence of Exogenous Photosensitizers. *Environ. Sci. Technol.* **2013**, *47*, 11004−11012.

(5) Chen, Y. M.; Lu, A. H.; Li, Y.; Zhang, L. S.; Yip, H. Y.; Zhao, H. J.; An, T. C.; Wong, P. K. Naturally Occurring Sphalerite as a Novel Cost-Effective Photocatalyst for Bacterial Disinfection under Visible Light. *Environ. Sci. Technol.* **2011**, *45*, 5689−5695.

(6) Matsunaga, T.; Tomoda, R.; Nakajima, T.; Wake, H. Photo-electrochemical Sterilization of Microbial Cells by Semiconductor Powders. *FEMS Microbiol. Lett.* **1985**, *29*, 211−214.

(7) Shannon, M. A.; Bohn, P. W.; Elimelech, M.; Georgiadis, J. G.; Marinas, B. J.; Mayes, A. M. Science and Technology for Water Purification in the Coming Decades. *Nature* **2008**, *452*, 301−310.

(8) Wang, W. J.; Ng, T. W.; Ho, W. K.; Huang, J. H.; Liang, S. J.; An, T. C.; Li, G. Y.; Yu, J. C.; Wong, P. K. CdIn₂S₄ Microsphere as an Efficient Visible-Light-Drive Photocatalyst for Bacterial Inactivation: Synthesis, Characterizations and Photocatalytic Inactivation Mechanisms. *Appl. Catal., B* **2013**, *129*, 482−490.

(9) Zhang, L. S.; Wong, K. H.; Yip, H. Y.; Hu, C.; Yu, J. C.; Chan, C. Y.; Wong, P. K. Effective Photocatalytic Disinfection of *E. coli* K-12 Using AgBr-Ag-Bi₂WO₆ Nanojunction System Irradiated by Visible Light: the Role of Diffusing Hydroxyl Radicals. *Environ. Sci. Technol.* **2010**, *44*, 1392−1398.

(10) Guo, M. T.; Huang, J. J.; Hu, H. Y.; Liu, W. J.; Yang, J. UV Inactivation and Characteristics after Photoreactivation of *Escherichia coli* with Plasmid: Health Safety Concern about UV Disinfection. *Water Res.* **2012**, *46*, 4031−4036.

(11) Wang, Q. H.; Kalantar-Zadeh, K.; Kis, A.; Coleman, J. N.; Strano, M. S. Electronics and Optoelectronics of Two-Dimensional Transition Metal Dichalcogenides. *Nat. Nanotechnol.* **2012**, *7*, 699−712.

(12) Sun, Z. Q.; Liao, T.; Dou, Y. H.; Hwang, S. M.; Park, M. S.; Jiang, L.; Kim, J. H.; Dou, S. X. Generalized Self-Assembly of Scalable Two-Dimensional Transition Metal Oxide Nanosheets. *Nat. Commun.* **2014**, *5*, 3813−3821.

(13) Yuan, J. J.; Li, H. D.; Wang, Q. L.; Yu, Q.; Zhang, X. K.; Yu, H. J.; Xie, Y. M. Fabrication, Characterization, and Photocatalytic Activity of Double-Layer TiO₂ Nanosheets Films. *Mater. Lett.* **2012**, *81*, 123−126.

(14) Chen, F. T.; Liu, Z.; Liu, Y.; Fang, P. F.; Dai, Y. Q. Enhanced Adsorption and Photocatalytic Degradation of High-Concentration Methylene Blue on Ag₂O-Modified TiO₂-Based Nanosheet. *Chem. Eng. J.* **2013**, *221*, 283−291.

(15) Ren, L.; Liu, Y. D.; Qi, X.; Hui, K. S.; Hui, K. N.; Huang, Z. Y.; Li, J.; Huang, K.; Zhong, J. X. An Architecture TiO₂ Nanosheet with Discrete Integrated Nanocrystalline Subunits and its Application in Lithium Batteries. *J. Mater. Chem.* **2012**, *22*, 21513−21518.

(16) Yi, T. F.; Fang, Z. K.; Xie, Y.; Zhu, Y. R.; Yang, S. Y. Rapid Charge-Discharge Property of Li₄Ti₅O₁₂-TiO₂ Nanosheet and Nano-tube Composites as Anode Material for Power Lithium-Ion Batteries. *ACS Appl. Mater. Interfaces* **2014**, *6*, 20205−20213.

(17) Chen, J. S.; Lou, X. W. Anatase TiO₂ Nanosheet: an Ideal Host Structure for Fast and Efficient Lithium Insertion/Extraction. *Electrochem. Commun.* **2009**, *11*, 2332−2335.

(18) Chen, F. T.; Fang, P. F.; Gao, Y. P.; Liu, Z.; Liu, Y.; Dai, Y. Q. Effective Removal of High-Chroma Crystal Violet over TiO₂-Based Nanosheet by Adsorption-Photocatalytic Degradation. *Chem. Eng. J.* **2012**, *204-206*, 107−113.

(19) Sun, J.; Zhang, H.; Guo, L. H.; Zhao, L. X. Two-Dimensional Interface Engineering of a Titania-Graphene Nanosheet Composite for Improved Photocatalytic Activity. *ACS Appl. Mater. Interfaces* **2013**, *5*, 13035−13041.

(20) Xiang, Q.; Lv, K.; Yu, J. Pivotal Role of Fluorine in Enhanced Photocatalytic Activity of Anatase TiO₂ Nanosheets with Dominant (001) Facets for the Photocatalytic Degradation of Acetone in Air. *Appl. Catal., B* **2010**, *96*, 557−564.

(21) Zhang, Y. X.; Yu, X. Y.; Jia, Y.; Jin, Z.; Liu, J. H.; Huang, X. J. A Facile Approach for the Synthesis of Ag-Coated Fe₃O₄@TiO₂ Core/Shell Microspheres as Highly Efficient and Recyclable Photocatalysts. *Eur. J. Inorg. Chem.* **2011**, *2011*, 5096−5104.

(22) Schneider, J.; Matsuoka, M.; Takeuchi, M.; Zhang, J. L.; Horiuchi, Y.; Anpo, M.; Bahnemann, D. W. Understanding TiO₂ Photocatalysis: Mechanisms and Materials. *Chem. Rev.* **2014**, *114*, 9919−9986.

(23) Chalasani, R.; Vasudevan, S. Cyclodextrin-Functionalized Fe₃O₄@TiO₂: Reusable, Magnetic Nanoparticles for Photocatalytic Degradation of Endocrine-Disrupting Chemicals in Water Supplies. *ACS Nano* **2013**, *7*, 4093−4104.

(24) Zhang, T.; Yan, X. L.; Sun, D. D. Hierarchically Multifunctional K-OMS-2/TiO₂/Fe₃O₄ Heterojunctions for the Photocatalytic Oxidation of Humic Acid under Solar Light Irradiation. *J. Hazard. Mater.* **2012**, *243*, 302−310.

(25) Liu, J. C.; Tsai, P. J.; Lee, Y. C.; Chen, Y. C. Affinity Capture of Uropathogenic *Escherichia coli* Using Pigeon Ovalbumin-Bound

$Fe_3O_4@Al_2O_3$ Magnetic Nanoparticles. *Anal. Chem.* **2008**, *80*, 5425–5432.

(26) Jin, Y. J.; Liu, F.; Shan, C.; Tong, M. P.; Hou, Y. L. Efficient Bacterial Capture with Amino Acid Modified Magnetic Nanoparticles. *Water Res.* **2014**, *50*, 124–134.

(27) Ryan, S.; Kell, A. J.; van Faassen, H.; Tay, L. L.; Simard, B.; Mackenzie, R.; Gilbert, M.; Tanha, J. Single-Domain Antibody-Nanoparticles: Promising Architectures for Increased Staphylococcus aureus Detection Specificity and Sensitivity. *Bioconjugate Chem.* **2009**, *20*, 1966–1974.

(28) Liu, L. H.; Dietsch, H.; Schurtenberger, P.; Yan, M. D. Photoinitiated Coupling of Unmodified Monosaccharides to Iron Oxide Nanoparticles for Sensing Proteins and Bacteria. *Bioconjugate Chem.* **2009**, *20*, 1349–1355.

(29) Li, C. Y.; Younesi, R.; Cai, Y. L.; Zhu, Y. H.; Ma, M. G.; Zhu, J. F. Photocatalytic and Antibacterial Properties of Au-Decorated $Fe_3O_4@mTiO_2$ Core-Shell Microspheres. *Appl. Catal., B* **2014**, *156–157*, 314–322.

(30) Xu, J. W.; Gao, Z. D.; Han, K.; Liu, Y. M.; Song, Y. Y. Synthesis of Magnetically Separable $Ag_3PO_4/TiO_2/Fe_3O_4$ Heterostructure with Enhanced Photocatalytic Performance under Visible Light for Photoinactivation of Bacteria. *ACS Appl. Mater. Interfaces* **2014**, *6*, 15122–15131.

(31) Chen, W. J.; Tsai, P. J.; Chen, Y. C. Functional Fe_3O_4/TiO_2 Core/Shell Magnetic Nanoparticles as Photokilling Agents for Pathogenic Bacteria. *Small* **2008**, *4*, 485–491.

(32) Ai, L. H.; Zhang, C. Y.; Chen, Z. L. Removal of Methylene Blue from Aqueous Solution by a Solvothermal-Synthesized Graphene/Magnetite Composite. *J. Hazard. Mater.* **2011**, *192*, 1515–1524.

(33) Lu, J.; Wang, M. Y.; Deng, C. H.; Zhang, X. M. Facile Synthesis of $Fe_3O_4@$Mesoporous TiO_2 Microsphere for Selective Enrichment of Phosphopeptides for Phosphoproteomics Analysis. *Talanta* **2013**, *105*, 20–27.

(34) Kim, D. S.; Kwak, S. Y. Photocatalytic Inactivation of *E. coli* with a Mesoporous TiO_2 Coated Film Using the Film Adhesion Method. *Environ. Sci. Technol.* **2009**, *43*, 148–151.

(35) Lin, H. X.; Deng, W. H.; Zhou, T. H.; Ning, S. B.; Long, J. L.; Wang, X. X. Iodine-Modified Nanocrystalline Titania for Photo-Catalytic Antibacterial Application under Visible Light Illumination. *Appl. Catal., B* **2015**, *176-177*, 36–43.

(36) Zhan, S. H.; Zhu, D. D.; Ma, S. L.; Yu, W. C.; Jia, Y. N.; Li, Y.; Yu, H. B.; Shen, Z. Q. Highly Efficient Removal of Pathogenic Bacteria with Magnetic Graphene Composite. *ACS Appl. Mater. Interfaces* **2015**, *7*, 4290–4298.

(37) Tong, T. Z.; Shereef, A.; Wu, J. S.; Binh, C. T. T.; Kelly, J. J.; Gaillard, J.; Gray, K. A. Effects of Materials Morphology on the Phototoxicity of Nano-TiO_2 to Bacteria. *Environ. Sci. Technol.* **2013**, *47*, 12486–12495.

(38) Bar-Ilan, O.; Chuang, C. C.; Schwahn, D. J.; Yang, S.; Joshi, S.; Pedersen, J.; Hamers, R. J.; Peterson, R. E.; Heideman, W. TiO_2 Nanoparticle Exposure and Illumination during Zebrafish Development: Mortality at Parts per Billion Concentrations. *Environ. Sci. Technol.* **2013**, *47*, 4726–4733.

(39) Liang, R. W.; Luo, S. G.; Jing, F. F.; Shen, L. J.; Qin, N.; Wu, L. A Simple Strategy for Fabrication of Pd@MIL-100(Fe) Nano-composite as a Visible-Light-Driven Photocatalyst for the Treatment of Pharmaceutical and Personal Care Products (PPCPs). *Appl. Catal., B* **2015**, *176-177*, 240–248.

(40) Huang, Y. F.; Wang, Y. F.; Yan, X. P. Amine-Functionalized Magnetic Nanoparticles for Rapid Capture and Removal of Bacterial Pathogens. *Environ. Sci. Technol.* **2010**, *44*, 7908–7913.

(41) Dalrymple, O. K.; Stefanakos, E.; Trotz, M. A.; Goswami, D. Y. A Review of the Mechanisms and Modeling of Photocatalytic Disinfection. *Appl. Catal., B* **2010**, *98*, 27–38.

(42) Applerot, G.; Lipovsky, A.; Dror, R.; Perkas, N.; Nitzan, Y.; Lubart, R.; Gedanken, A. Enhanced Antibacterial Activity of Nanocrystalline ZnO due to Increased ROS-Mediated Cell Injury. *Adv. Funct. Mater.* **2009**, *19*, 842–852.

(43) Imlay, J. A.; Linn, S. Mutagenesis and Stress Responses Induced in *Escherichia coli* by Hydrogen Peroxide. *J. Bacteriol.* **1987**, *169*, 2967–2976.

(44) Kawarai, T.; Wachi, M.; Ogino, H.; Furukawa, S.; Suzuki, K.; Ogihara, H.; Yamasaki, M. SulA-Independent Filamentation of *Escherichia coli* during Growth after Release from High Hydrostatic Pressure Treatment. *Appl. Microbiol. Biotechnol.* **2004**, *64*, 255–262.

(45) Kumar, S.; Surendar, T.; Kumar, B.; Baruah, A.; Shanker, V. Synthesis of Magnetically Separable and Recyclable g-C_3N_4-Fe_3O_4 Hybrid Nanocomposites with Enhanced Photocatalytic Performance under Visible-Light Irradiation. *J. Phys. Chem. C* **2013**, *117*, 26135–26143.

(46) Schrank, S. G.; Jose, H. J.; Moreira, R. F. P. M. Simultaneous Photocatalytic Cr(VI) Reduction and Dye Oxidation in a TiO_2 Slurry Reactor. *J. Photochem. Photobiol., A* **2002**, *147*, 71–76.

(47) Amine-Khodja, A.; Boulkamh, A.; Richard, C. Phototransformation of Metobromuron in the Presence of TiO_2. *Appl. Catal., B* **2005**, *59*, 147–154.

(48) Jin, R.; Gao, W.; Chen, J.; Zeng, H.; Zhang, F.; Liu, Z.; Guan, N. Photocatalytic Reduction of Nitrate Ion in Drinking Water by Using Metal-Loaded $MgTiO_3$-TiO_2 Composite Semiconductor Catalyst. *J. Photochem. Photobiol., A* **2004**, *162*, 585–590.

(49) Wang, W. J.; Yu, Y.; An, T. C.; Li, G. Y.; Yip, H. Y.; Yu, J. C.; Wong, P. K. Visible-Light-Driven Photocatalytic Inactivation of *E. coli* K-12 by Bismuth Vanadate Nanotubes: Bactericidal Performance and Mechanism. *Environ. Sci. Technol.* **2012**, *46*, 4599–4606.

(50) Wang, W. J.; Zhang, L. Z.; An, T. C.; Li, G. Y.; Yip, H. Y.; Wong, P. K. Comparative Study of Visible-Light-Drive Photocatalytic Mechanisms of Dye Decolorization and Bacterial Disinfection by B-Ni-Codoped TiO_2 Microspheres: the Role of Different Reactive Species. *Appl. Catal., B* **2011**, *108-109*, 108–116.